A Time-Scale Decomposition Approach to Statistically Downscale Summer Rainfall over North China

YAN GUO

State Key Laboratory of Numerical Modeling for Atmospheric Sciences and Geophysical Fluid Dynamics, Institute of Atmospheric Physics, Chinese Academy of Sciences, and Graduate University of Chinese Academy of Sciences, and Key Laboratory of Earth Surface Processes and Resource Ecology, Beijing Normal University, Beijing, China

JIANPING LI

State Key Laboratory of Numerical Modeling for Atmospheric Sciences and Geophysical Fluid Dynamics, Institute of Atmospheric Physics, Chinese Academy of Sciences, Beijing, China

YUN LI

CSIRO Mathematics, Informatics and Statistics, Wembley, Western Australia, Australia

(Manuscript received 31 December 2010, in final form 2 June 2011)

ABSTRACT

A time-scale decomposition (TSD) approach to statistically downscale summer rainfall over North China is described. It makes use of two distinct downscaling models respectively corresponding to the interannual and interdecadal rainfall variability. The two models were developed based on objective downscaling scheme that 1) identifies potential predictors based on correlation analysis between rainfall and considered climatic variables over the global scale and 2) selects the ''optimal'' predictors from the identified potential predictors via cross-validation-based stepwise regression. The downscaling model for the interannual rainfall variability is linked to El Niño–Southern Oscillation and the 850-hPa meridional wind over East China, while the one for the interdecadal rainfall variability is related to the sea level pressure over the southwest Indian Ocean. Taking the downscaled interannual and interdecadal components together the downscaled total rainfall was obtained. The results show that the TSD approach achieved a good skill to predict the observed rainfall with the correlation coefficient of 0.82 in the independent validation period. The authors further apply the model to obtain downscaled rainfall projections from three climate models under present climate and the A1B emission scenario in future. The resulting downscaled values provide a closer representation of the observation than the raw climate model simulations in the present climate; for the near future, climate models simulated a slight decrease in rainfall, while the downscaled values tend to be slightly higher than the present state.

1. Introduction

In the past decades, global climate has undergone rapid changes as it has been approved by documented observation in every continent (Solomon et al. 2007). Projection for future climate (e.g., rainfall) and its associated influences on environment and society (e.g., runoff and water storages) have attracted growing attentions worldwide. However, uncertainties in projected rainfall changes for later this century plague estimates of impacts on future runoff and water storages (Milly et al. 2008). In particular, there are several difficulties associated with interpreting changes in variables simulated at a resolution of 100–200 km in terms of changes to be expected at smaller catchment scales. There is an increasing demand for more reliable estimates of these changes by water resource managers who need to make long-term decisions about future infrastructure demands (e.g., new reservoirs, pipelines, drainage, etc.). North China (NC; 110°–122°E, 35°–40°N) has already been severely affected by a downturn

Corresponding author address: Dr. Jianping Li, State Key Laboratory of Numerical Modeling for Atmospheric Sciences and Geophysical Fluid Dynamics, Institute of Atmospheric Physics, Chinese Academy of Sciences, Beijing 100029, China.
E-mail: ljp@lasg.iap.ac.cn

DOI: 10.1175/JCLI-D-11-00014.1

in rainfall and reductions in runoff and water shortage. Problems of water shortage and related environmental issues in NC have become the most significant limiting factors affecting sustainable development in this important region of China (Xia et al. 2007).

NC is located at the northern margin of East Asian subtropical monsoon region and receives the bulk of annual rainfall during the summer half-year (i.e., May–October). Summer (July–August) rainfall over NC is affected by both the teleconnected large-scale signals and the regional signals. As for the teleconnected signals, El Niño–Southern Oscillation (ENSO) was reported to be associated with NC summer rainfall (Huang and Wu 1989; Lu 2005; Wang et al. 2000; Wu and Li 2008); North Atlantic Oscillation (NAO) yields another predictability source for the NC summer rainfall (Wu et al. 2009, 2011). Additionally, the regional signals, such as the components in the East Asian summer monsoon (EASM) system (Huang et al. 2008; Li and Zeng 2002; Yang and Sun 2003) and the mid-high-latitude circulations over Eurasia (Wang et al. 2008; Zhao and Song 1999) also exert influence on NC summer rainfall. Lu (2002, 2003) reported that there exists obviously distinct variability at the interannual and interdecadal time scales in NC summer rainfall. The strong high-frequency variability results in severe floods or droughts in NC (Huang et al. 2006), while the low-frequency variability shows a pronounced drying trend during the past half-century, which has attracted great interests to find out the underlying causes of the multidecadal drought over NC (Ding et al. 2009; Li et al. 2010; Li et al. 2003; Sun 1999; Zhou et al. 2009a). The extremely complex variability in NC summer rainfall complicates its seasonal prediction and long-term projections. This is an important issue in terms of disaster prevention and mitigation and decision making.

It is well-known that general circulation models (GCMs) provide a good tool to project the large-scale long-term mean future climate; however, the skillful spatial resolution in most updated climate models is large than or at least 2000–4000 km (Grotch and MacCracken 1991), beyond the demand for regional precipitation prediction, which is sensitive to subgrid processes. The physical parameterization schemes are critical for precipitation projection, and the limitation of parameterization schemes in current climate models is also responsible for the large uncertainties in rainfall simulations, even for ensemble forecasts (Whetton et al. 2005).

Many approaches have been developed to overcome the uncertainties accompanying future rainfall projections, including the assessment of the performance of individual models as a guide to the reliability of their predicted changes (Maxino et al. 2008; Perkins et al. 2007; Smith and Chandler 2009; Wu and Li 2009). Statistical downscaling is another method that can potentially assist in the assessment of climate models. A simple test for a model is that it cannot only provide an accurate estimate for regional rainfall, but that it should also simulate the observed relationship between regional rainfall and other key variables, for example, sea level pressure (SLP). If these criteria can be satisfied, simulated changes in rainfall are more likely reliable than otherwise. It cannot only provide an indication of any such relationship, it can also potentially provide alternative estimates for rainfall changes if the model-simulated changes in the key variables are believed to be more reliable than the rainfall estimates themselves (Benestad 2001).

Statistical downscaling is an empirical relationship between the large-scale climate anomalies and local climate fluctuations based on historical data. There are numerous ways to develop statistical downscaling models (Fowler et al. 2007), but it is important to note that a statistical downscaling approach assumes that any derived historical relationship also holds for the future (Wilby 1997).

Among various statistical downscaling models, multiple linear regression models built using gridcell values of atmospheric variables as predictors for surface temperature and precipitation are popular because of their simplicity and explicit physical meaning (Benestad 2001; Wilby 1998). Other more complex techniques include using the principal components (PCs) of pressure fields or geopotential height fields (Hanssen-Bauer and Forland 1998; Kidson and Thompson 1998; Li and Smith 2009) and more sophisticated methods such as canonical correlation analyses (Busuioc et al. 2001; Karl et al. 1990; Von Storch et al. 1993), singular value decomposition (Zhu et al. 2008), and partial least squares regression (Bergant and Kajfe-Bogataj 2005).

There is no doubt that the choice of predictors and the associated domains plays a key role in statistical downscaling. An amount of sensitivity studies have indicated that the choice of predictors and domains is critical for future projections (Benestad 2001; Frias et al. 2006; Schmidli et al. 2007). The commonly used predictors are derived from circulation parameters, which could be credibly simulated by GCMs, including SLP, geopotential heights, horizontal winds at various levels, etc. For the choice of predictor domains, its importance has been indicated (Benestad 2001; Wilby and Wigley 2000), but this issue of how to choose has not been systematically addressed in the existing studies. The common approach is to subjectively select a fixed domain that encompasses the target location of the predictand (Oshima et al. 2002; Timbal et al. 2003) or to select the best from several trial

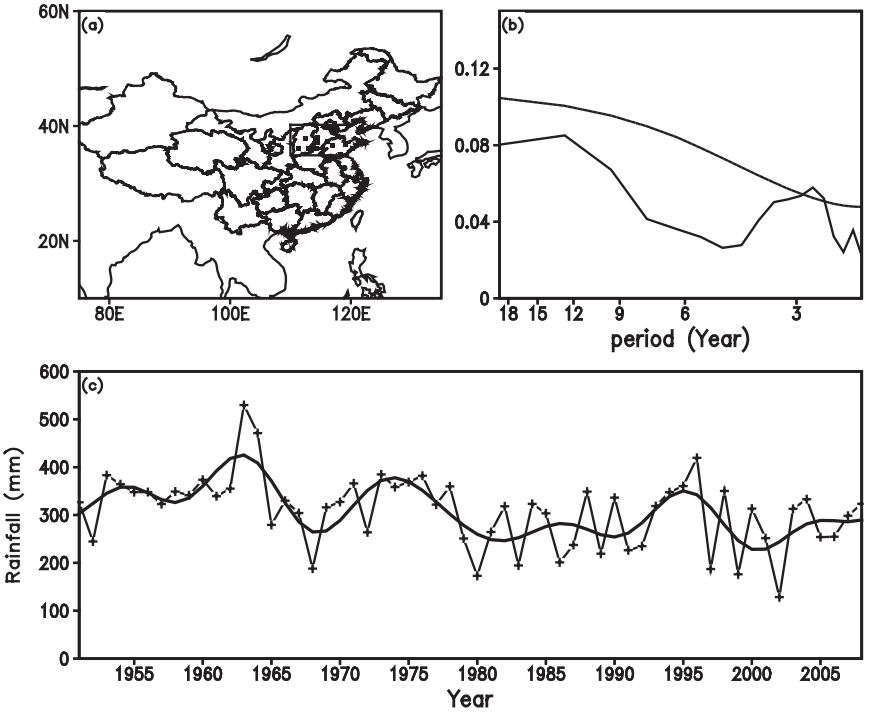

FIG. 1. (a) The 15 gauge stations used to represent North China (110°–122°E, 35°–40°N) denoted by the rectangle. (b) Power spectrum for July–August rainfall. Peak over the dashed line indicates the confidence level is > 80% against a red noise. (c) Total rainfall (mm) during July–August (+'s) from 1951 to 2008 and its interdecadal variation with period exceeding 7 years (solid line).

domains that surrounds the target location with contrasting locations and spatial extensions (Benestad 2001, 2002). Benestad (2004) first proposed a quantitative rule to determine the spatial extent of domain surrounding the target position. It examined the correlation map between climatic parameter over the target position and the surrounding areas and defined the domain according to where the correlation goes to zero. Nevertheless, this proposition only considers the effect of the local and nearby systems but misses the remote predictive signals that exert an influence via teleconnection. Because the teleconnection is an atmospheric phenomenon explained by spherical planetary wave propagation theory (Hoskins and Karoly 1981); consequently, the preceding or concurrent teleconnection signals is useful for statistical predictions. Therefore, it is intuitive to identify potential predictors over the global scale.

The aim of this work is to build a statistical downscaling model for NC summer rainfall using an objective approach that objectively selects potential predictors over the global scale. Given that there are significantly distinct components in rainfall variability at the interannual and interdecadal time scales, it is desirable to develop a time-scale decomposition (TSD) approach to obtain the downscaled rainfall totals by combining two distinct downscaling models for the interannual and interdecadal rainfall variability.

The framework of this study is organized as follows. Section 2 introduces the data used in this work. Section 3 describes the proposed TSD approach to statistically downscale NC summer rainfall. The downscaled results from two distinct statistical downscaling models calibrated for the interannual and interdecadal rainfall variability and their combined results for total rainfall are presented in section 4. Key results by applying the downscaling model to climate change simulations are described in section 5. Finally, section 6 contributes to a summary and discussion.

2. Data

Observed rainfall data were derived from 160-station monthly rainfall dataset for China provided by the China Meteorological Administration for the period 1951–2008. July and August (JA) is the primary rainy season over NC, and the total rainfall series during JA averaged over 15 gauge stations (Fig. 1a) within the region of 110°–122°E, 35°–40°N is designed to be predicted.

Atmospheric data were extracted from the National Centers for Environment Prediction (NCEP)–National Center for Atmospheric Research (NCAR) reanalysis dataset on a 2.5° × 2.5° grid (http://www.esrl.noaa.gov/psd/data/gridded/data.ncep.reanalysis.html), including SLP, 500-hPa geopotential height (Z500), 850-hPa meridional wind (V850), etc. SST data were taken from Hadley Center SST dataset I on a 1° × 1° grid (http://hadobs.metoffice.com/hadisst/). Several well-known climate indices are employed as candidate predictors. The southern annular mode index (SAMI) is defined as the difference in the normalized monthly zonal-mean SLP between 40° and 70°S (Nan and Li 2003), and the northern annular mode index (NAMI) is defined as the difference between 35° and 65°N (Li and Wang 2003a), both are available online (http://web.lasg.ac.cn/staff/ljp/dataset.html). The North Atlantic Oscillation index (NAOI) is defined similar to NAMI but regionally over the North Atlantic sector from 80°W to 30°E (Li and Wang 2003b); it is also available online (http://web.lasg.ac.cn/staff/ljp/dataset.html). The Niño-3 index is used to represent the ENSO phenomenon and available online (http://www.cpc.noaa.gov/data/indices). The Pacific decadal oscillation index (PDOI) is derived as the leading PC of monthly SST anomalies in the North Pacific Ocean poleward of 20°N (Zhang et al. 1997) and is available online (http://jisao.washington.edu/pdo/PDO.latest).

The GCM data were derived from three GCMs [Commonwealth Scientific and Industrial Research Organisation Mark version 3.5 (CSIRO Mk3.5), Centre National de Recherches Météorologiques Coupled Global Climate Model, version 3 (CNRM-CM3), and Max Planck Institute (MPI) ECHAM5] selected from 21 GCMs (Table 1) participating in the World Climate Research Programme's (WCRP's) Coupled Model Intercomparison Project phase 3 (CMIP3) due to their simulation of the predictors in the downscaling model. The outputs from the twentieth-century simulation experiment (20c3m) and climate change experiment based on the A1B emission scenario of Intergovernmental Panel on Climate Change (IPCC) Assessment Report 4 (AR4) are utilized and they are available online (http://www-pcmdi.llnl.gov/). Since these GCMs have different horizontal resolutions, raw GCMs outputs were interpolated into a resolution of 2.5° × 2.5° the same as NCEP reanalysis data using bilinear interpolation method.

3. Methods

The spectrum analysis shows that there primarily exist two peaks with periods of 2–3 years and 12–15 years in the NC summer rainfall during 1951–2008 (Fig. 1b), indicating strong interannual and interdecadal variability (Fig. 1c). A previous study (Lu 2003) indicated that there are distinct relationships between the NC summer rainfall and circulation anomalies at the interdecadal and interannual time scales, respectively; the interdecadal variation does not modify the interannual variation and its physical mechanism. This finding motivates us to build a TSD approach to downscale NC summer rainfall by identifying respective forcing factors linked to the interannual and interdecadal variability via distinct statistical-downscaling models, respectively.

The main stages to establish and validate the TSD model are shown in Fig. 2. Assume that the observed rainfall series $Y(t)$ can be decomposed into the interannual component $Y_A(t)$ and the interdecadal component $Y_D(t)$ by

$$Y(t) = Y_A(t) + Y_D(t). \quad (1)$$

To establish a TSD approach to downscale rainfall $Y(t)$, the whole study period 1951–2008 ($N = 58$) was separated into the calibration period 1951–90 ($n = 40$) and independent validation period 1991–2008.

To calibrate models for the interannual and interdecadal rainfall variability, observed rainfall and individual predictors are decomposed as the interannual (variation less than 7 years) and interdecadal (variation longer than 7 years) components by Fourier decomposition filtering using the data over 1951–90. A correlation-based cross-validation stepwise regression (C_CVSR) downscaling scheme documented in our previous paper (Guo et al. 2011, manuscript submitted to *J. Geophys. Res.*) is used to build the interannual model (IAM) and interdecadal model (IDM) for the relationship between rainfall and associated predictors at interannual and interdecadal time scales, respectively. Taking the predicted values $\hat{Y}_A(t)$ and $\hat{Y}_D(t)$ together we obtain the predicted rainfall totals over the training period 1951–90. Note that the C_CVSR downscaling scheme primarily contains two stages—that is, 1) the identification of potential predictors over the global scale through correlation analysis with rainfall, and 2) the selection of ''optimal'' predictors from the potential predictor set to formulate regression equations by cross-validation-based stepwise regression (CVSR) approach. See appendix A for some details about the CVSR approach.

To validate the skill of the TSD approach to downscale NC summer rainfall, predictors selected by the IAM and IDM based on the training period 1951–90 are decomposed as the interannual and interdecadal components by Fourier decomposition filtering over the whole period 1951–2008 ($N = 58$), and they are taken into respective forecast equation (the IAM and IDM)

TABLE 1. List of the 21 GCMs used in our study.

Name	Research Group	Horizontal resolution	Run
Bjerknes Center for Climate Research (BCCR) Bergen Climate Model version 2 (BCM2.0)	Bjerknes Center for Climate Research, Norway	T63	run1
Canadian Centre for Climate Modelling and Analysis (CCCma) Coupled General Circulation Model, version 3.1 (CGCM3.1) (T47)	Canadian Centre for Climate Modeling and Analysis, Canada	T47	run1
CGCM3.1(T63)	Canadian Centre for Climate Modeling and Analysis, Canada	T63	run1
CNRM-CM3	Meteo-France/Center National de Recherches Meteorologiques, France	T63	run1
CSIRO Mk3.0	CSIRO Atmospheric Research, Australia	T63	run1
CSIRO Mk3.5	CSIRO Atmospheric Research, Australia	T63	run1
Institute of Atmospheric Physics (IAP) Flexible Global Ocean–Atmosphere–Land System Model gridpoint version 1.0 (FGOALS1.0)	State Key Laboratory of Numerical Modeling for Atmospheric Sciences and Geophysical Fluid Dynamics (LASG)/Institute of Atmospheric Physics, China	2.8 × 2.8	run1
Geophysical Fluid Dynamics Laboratory Climate Model version 2.0 (GFDL CM2.0)	National Oceanic and Atmospheric Administration (NOAA) Geophysical Fluids Dynamics Laboratory, United States	2 × 2.5	run1
GFDL_CM2.1	NOAA Geophysical Fluids Dynamics Laboratory, United States	2 × 2.5	run1
Goddard Institute for Space Studies Atmosphere–Ocean Model (GISS-AOM)	National Aeronautics and Space Administration (NASA) Goddard Institute for Space Studies, United States	3 × 4	run1
GISS Model E-H (GISS-EH)	NASA Goddard Institute for Space Studies, United States	4 × 5	run1
GISS Model E-R (GISS-ER)	NASA Goddard Institute for Space Studies, United States	4 × 5	run1
Institute of Numerical Mathematics Coupled Model, version 3.0 (INM-CM3.0)	Institute for Numerical Mathematics, Russia	4 × 5	run1
Istituto Nazionale di Geofisica e Vulcanologia (Italy) GCM version SXG (INGV-SXG)	Instituto Nazionale di Geofisica e Vulcanologia	T106	run1
Model for Interdisciplinary Research on Climate 3.2, high-resolution version [MIROC3.2(hires)]	Center for Climate Research Studies (CCSR) of Tokyo University, Frontier of the Japan Agency for Marine-Earth Science and Technology (JAMSTEC), Japan	T106	run1
MIROC3.2 medium resolution version [MIROC3.2(medres)]	CCSR of Tokyo University, Frontier of JAMSTEC, Japan	T106	run1
MPI ECHAM5	Max Plank Institute for Meteorology, Germany	1.5 × 1.5	run1
Meteorological Research Institute Coupled General Circulation Model, version 2.3.2 (MRI CGCM2.3.2)	Meteorological Research Institute, Japan	T42	run1
NCAR Community Climate System Model, version 3 (CCSM3.0)	National Center for Atmospheric Research, United States	T85	run1
Third climate configuration of the Met Office (UKMO) Unified Model (HadCM3)	Hadley Center for Climate Prediction and Research/Met Office, United Kingdom	2.75 × 3.75	run1
UKMO Hadley Centre Global Environmental Model version 1 (HadGEM1)	Hadley Center for Climate Prediction and Research/Met Office, United Kingdom	1.25 × 1.875	run1

to calculate the downscaled interannual and interdecadal rainfall components over the validation period 1991–2008. Taking the predicted values $\hat{Y}_A(t)$ and $\hat{Y}_D(t)$ from the IAM and IDM together, we obtain the predicted rainfall totals over 1991–2008, which indicate the true predictive skill of the TSD approach. We quantify the degree of prediction uncertainty with the bootstrap approach (Stine 1985), and the confidence intervals associated with the prediction are derived from the spread of 1000 bootstrap samples with random replacement. See appendix B for some details about the bootstrap approach.

4. Downscaling NC summer rainfall

In this section, we use C_CVSR downscaling scheme to establish distinct models for relationships between distinct large-scale predictors and the NC summer rainfall at the interannual and interdecadal time scales, respectively.

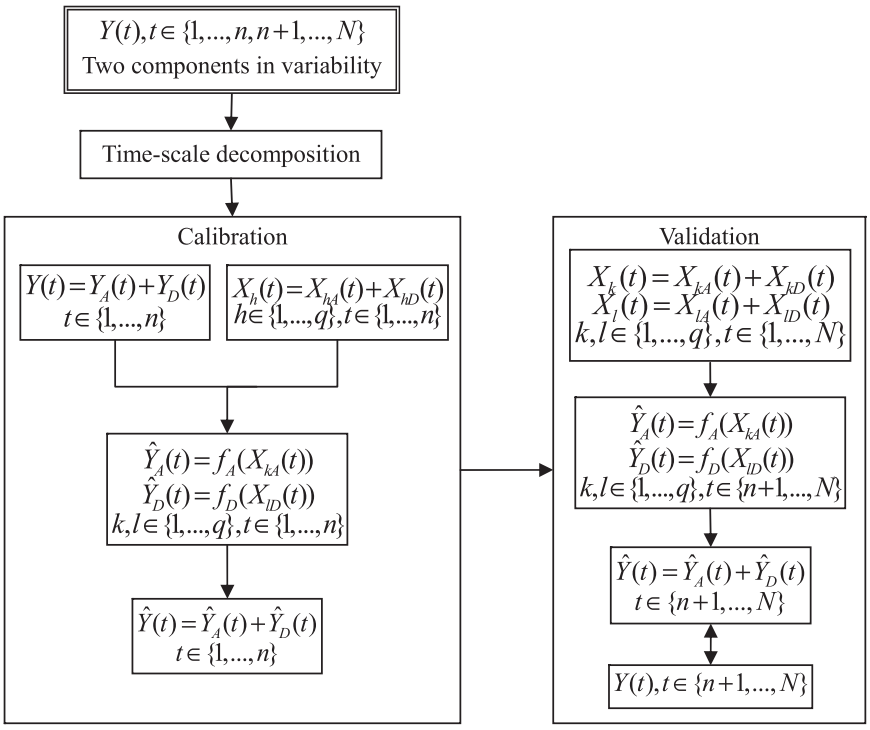

FIG. 2. Key stages in calibrating and validating the time-scale decomposition downscaling model.

a. Calibrating the IAM

The interannual correlation between the well-known climate indices and NC summer rainfall are shown in Table 2. It seems that the interannual components of the June NAOI (NAO_A) and Niño-3 index ($Niño3_A$) are significantly relevant, thus, these two indices are taken as candidate predictors for modeling the interannual rainfall variability. To further seek other possible predictors over global scale, interannual correlation of the detrended time series between SLP, V850, Z500, SST fields, and rainfall during 1951–90 is calculated (Fig. 3). Previous studies indicated that interannual rainfall is associated with the circulation systems including low-level meridional wind over East China (Huang et al. 1999), mid-high circulation over Eurasia (Zhao and Song 1999), the Mascarene high and Australian high (Xue 2005), and the Somali Jet (Wang and Xun 2003); indeed, high correlation coefficients appear over these areas, as indicated by the rectangles in Fig. 3. Potential predictors associated with the interannual rainfall variability are calculated by averaging the values over the areas having correlation coefficients exceeding 0.4 (significant at the 0.01 level) within the marked rectangles, which are denoted as $Z_{1A}-Z_{9A}$, and their details are listed in Table 3. It is clear that each of these nine potential predictors has a strong link with the NC summer rainfall with the significant correlation coefficient at the 0.01 level.

Figure 4a shows the whole process of CVSR screening procedure in calibrating the IAM. The root-mean-square-error (RMSE) between the observed and cross-validation estimated rainfall (CV_RMSE) is used to measure the predictive performance of potential predictors at each step. Since the well-known teleconnection indices represent large-scale signals and possess explicit physical meaning, the significantly related indices (NAO_A

TABLE 2. Interannual (interdecadal) correlation of detrended time series between July–August rainfall and several indices in June and July–August (JA) during 1951–90.

	SAMI	NAMI	NAOI	PDOI	Niño-3 index
June	−0.06(−0.83*)	−0.27(0.04)	−0.37**(0.19)	0.12(−0.66*)	−0.35**(−0.52)
JA	−0.09(−0.54**)	0.08(−0.37)	0.24(−0.31)	−0.25(−0.54*)	−0.29(−0.12)

* Significant at the 0.05 level.
** Significant at the 0.01 level.

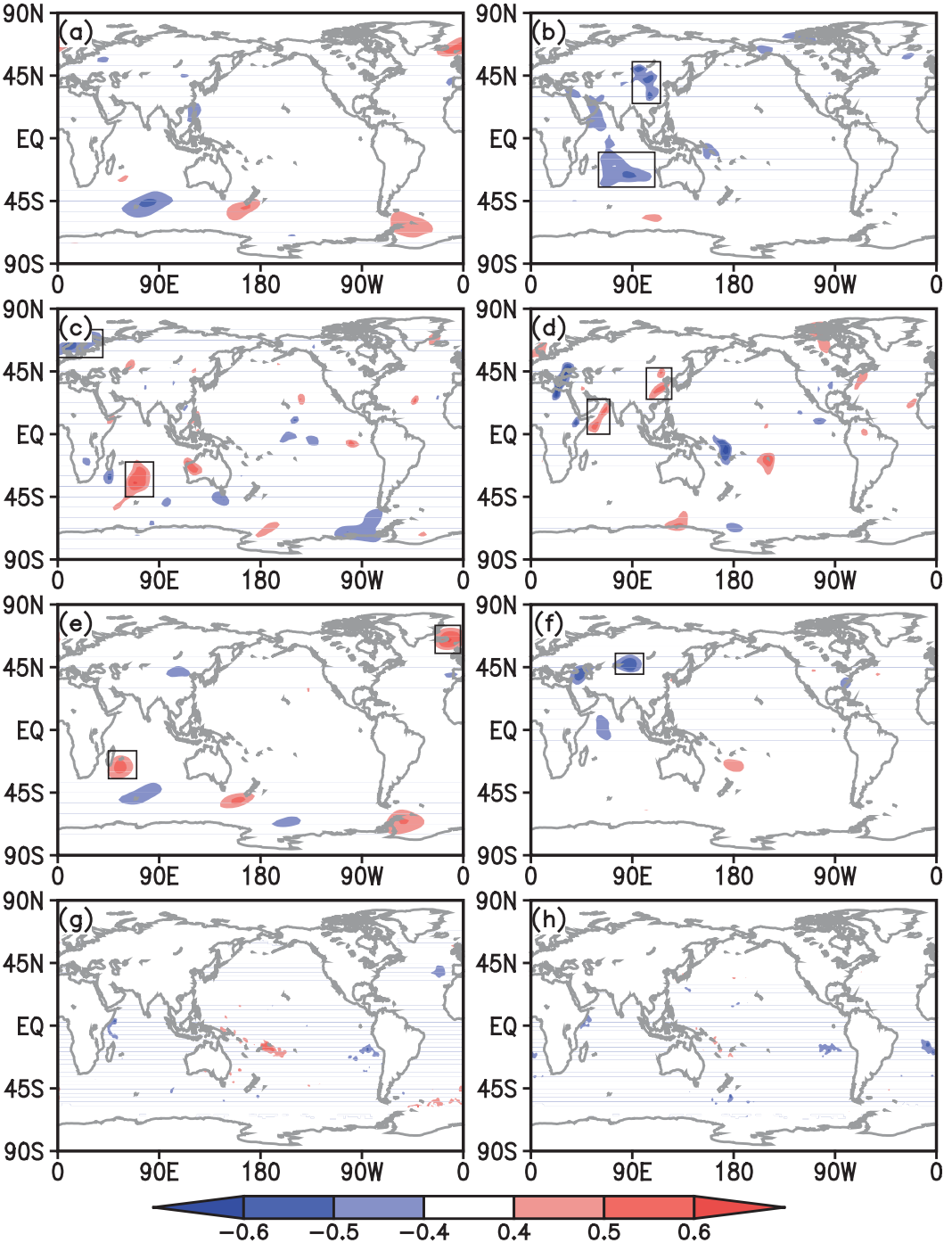

FIG. 3. Interannual correlation of detrended time series between July–August rainfall and (a),(b) sea level pressure, (c),(d) 850-hPa meridional wind, (e),(f) 500-hPa geopotential height, and (g),(h) sea surface temperature in (left) June and (right) July–August during 1951–90. Color shading indicates statistical significance at the 0.01 level. Black rectangles indicate areas with high correlation coefficients.

and Niño3_A) are preferentially taken to be selected in CVSR procedure. At step 1, Niño3_A is selected since it yields the smaller CV_RMSE value of 49.9 mm. At step 2, the CV_RMSE shows a decrease after adding the NAO_A, but this decrease in quadratic error is not statistically significant in terms of the mean value and the variance value because the *t*- and *F*-tests' values are 0.33 and 1.1, less than the significant values of 1.4 and 1.6 at

TABLE 3. Definitions of potential predictors for interannual model (IAM) and interdecadal model (IDM) and their correlation with rainfall on the respective time scales for the period 1951–90.

Model	Parameter	Level	Month	Area of surrounding rectangle	Label	Correlation (1951–1990) Raw	Detrended
IAM	Sea level pressure	Surface	JA	25°–55°N, 90°–115°E	Z_{1A}	−0.57	−0.57
	Sea level pressure	Surface	JA	35°–10°S, 60°–110°E	Z_{2A}	−0.52	−0.52
	Meridional wind	850 hPa	June	45°–20°S, 60°–85°E	Z_{3A}	0.58	0.59
	Meridional wind	850 hPa	June	55°–75°N, 0°–40°E	Z_{4A}	−0.6	−0.6
	Meridional wind	850 hPa	JA	25°–47.5°N, 102.5°–125°E	Z_{5A}	0.64	0.65
	Meridional wind	850 hPa	JA	0°–25°N, 50°–70°E	Z_{6A}	0.62	0.62
	Geopotential height	500 hPa	June	35°–15°S, 45°–70°E	Z_{7A}	0.51	0.5
	Geopotential height	500 hPa	June	55°–75°N, 335°–357.5°E	Z_{8A}	0.62	0.62
	Geopotential height	500 hPa	JA	40°–55°N, 75°–100°E	Z_{9A}	−0.59	−0.59
IDM	Sea level pressure	Surface	June	25°S–10°N, 30°–60°E	Z_{1D}	−0.95	−0.94
	Sea level pressure	Surface	JA	30°S–10°N, 30°–80°E	Z_{2D}	−0.93	−0.92
	Geopotential height	500 hPa	June	5°S–20°N, 90°–140°E	Z_{3D}	−0.94	−0.92
	Geopotential height	500 hPa	June	5°–35°N, 50°–90°E	Z_{4D}	−0.92	−0.9

the 0.15 level. Among the well-known indices, only Niño3$_A$ is selected into the regression equation. The additional potential predictors ($Z_{1A} - Z_{9A}$) are added to be selected at the following steps. At step 3, the sequential inclusion of Z_{5A}results in a statistically significant reduction in the CV_RMSE value to the minimum of 39.3 mm (t- and F-tests' values are 1.5 and 1.62, exceeding the significant values); thus, Z_{5A} is selected into the regression equation as the second predictor. At step 4, further inclusion of Z_{8A} reduces the CV_RMSE value to a minimum of 33.2 mm; however, this reduction in quadratic error is not statistically significant, indicating termination of the CVSR screening procedure.

As a result of the CVSR screening procedure, Niño3$_A$ and Z_{5A} are finally selected into regression equation as predictors X_{1A} and X_{2A}; in both cases, their regression coefficients are significant at the 0.05 level. The IAM is finally given in the form of

$$Y_A(t) = -14X_{1A}(t) + 31.1X_{2A}(t), \qquad (2)$$

where $Y_A(t)$ is the interannual component of rainfall at tth year ($t = 1, \ldots, 40$) over 1951–90, $X_{1A}(t)$ and $X_{2A}(t)$ are the tth-observed values of the normalized indices X_{1A} and X_{2A}.

Figure 5a shows the interannual variation of observed and downscaled rainfall from the IAM (2). The IAM provides a relatively accurate representation of observations, even for the independent verification period. Table 4 summarizes this skill by showing the correlation coefficients, RMSE and the ratio of RMSE to the climatology rainfall (base period 1951–2008) between the downscaled and observed values. The correlation coefficient and RMSE are 0.76 and 34.2 mm (11.1%) in training period and 0.71 and 42.8 mm (13.9%) in independent validation period.

As a physically meaningful downscaling model, the relationship between the predictors and rainfall should be physically interpretable. In this regard, we explore the possible physical linkage between the interannual rainfall variation and predictors X_{1A} and X_{2A} by using the data from the whole period 1951–2008.

The first predictor X_{1A} is the interannual component of the June Niño-3 index, representing the interannual variation in June SST over the mideastern tropical Pacific. When there is anomalous warming (i.e., positive X_{1A} anomaly), large-scale anomalous cooling appears over the western tropical Pacific, and this anomalous El Niño pattern could persist throughout JA (Fig. 6a). As an atmospheric Rossby wave response to the western Pacific large-scale cooling in the western tropical Pacific, an anomalous meridional tripole pattern is induced at the low–midtroposphere over the western Pacific (Fig. 6b), which is analogous to the Pacific–Japan or East Asia–Pacific teleconnection pattern. Figures 6c,d show the horizontal and meridional circulation response as follows: anomalously strong WPSH locates at about 25°N, and an anomalous northeasterly at its southern boundary encounters northeastward cross-equator flows, giving rise to anomalous convergence and ascent; at its northwestern boundary, anomalous northward flows encounters the southward flows induced by the cyclonic anomaly over the North Pacific and northeast Asia, leading to anomalous convergence and ascent at about 32°N. This anomalous circulation structure, which is consistent with previous studies (Huang and Wu 1989; Lu 2005; Nitta 1987), makes NC under the influence of cold and dry flows descending from Northeast Asia and suppresses precipitation occurring over NC. In contrast, when there is an anomalous cooling over the mideastern tropical Pacific in June (i.e., negative X_{1A} anomaly), the circulation described above would reverse, favoring a wet summer over NC.

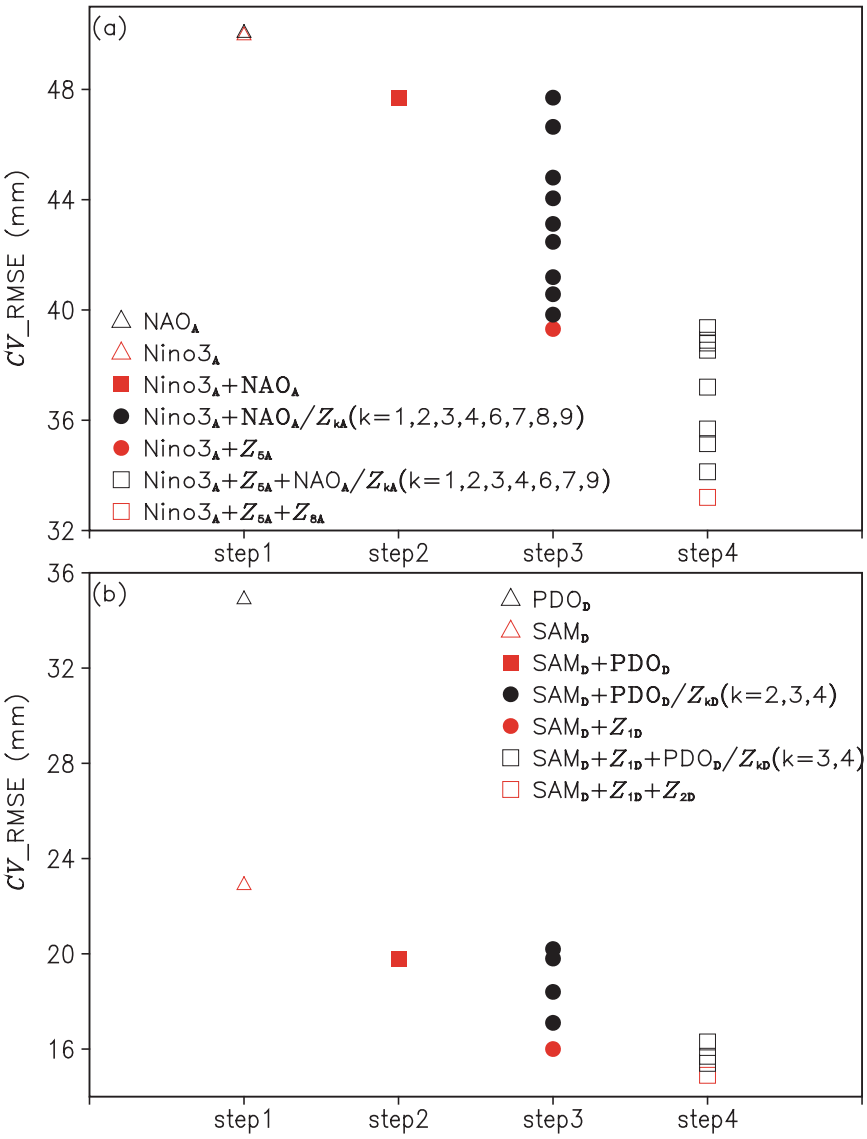

FIG. 4. Root-mean-square error between observed and cross-validation-estimated rainfall (CV_RMSE; mm) by different potential predictors (legend) in each step of stepwise regression procedure for (a) interannual model and (b) interdecadal model. The red markers denote the minimum CV_RMSE value in each step. For definitions of the potential predictors Z_{1A}–Z_{9A} and Z_{1D}–Z_{4D}, see text.

The second predictor X_{2A} represents the interannual component of JA meridional wind over East China at 850 hPa, which is a regional predictor. Figure 7 shows the interannual correlation of the detrended time series between the negative X_{2A} and geopotential height at 850, 500, and 200 hPa. It is evident that, associated with $-X_{2A}$, there appears a quasi-barotropic anomaly in geopotential height fields of an anticyclonic anomaly over central Asia and Mongolia region and a cyclonic anomaly over northwestern Pacific corresponding to the anomalous northeasterly over East China. As a result, the anomalous northeasterly currents prevent warm and moist air being transferred to the NC, leading to a dry summer. Thus, NC summer rainfall is closely associated with low-level meridional wind at interannual time scale, and it modulates the transfer of warm and humid air from South China Sea and western Pacific. This result is consistent with the previous study by Huang et al. (1999). Yet the underlying driver for the quasi-barotropic pressure anomaly in low–mid–high troposphere is not clear and deserves further investigation.

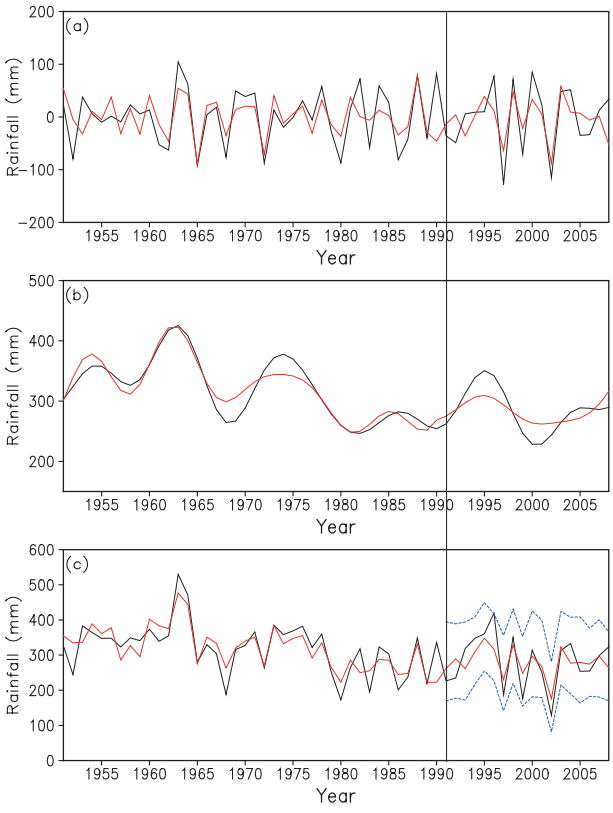

FIG. 5. (a) Interannual component, (b) interdecadal component, and (c) total amount of the observed (black solid line) and downscaled (red solid line) July–August rainfall (mm) during training period (1951–90) and test period (1991–2008). Blue-dashed lines denote 95% confidence intervals.

b. *Calibrating the IDM*

The procedure for calibrating the IDM is the same as that for IAM. The June SAMI and PDOI show significant correlations with rainfall at interdecadal time scale (Table 2); thus, the interdecadal components of SAMI (SAM_D) and PDOI (PDO_D) are considered as candidate predictors for IDM. Figure 8 shows the interdecadal correlation of detrended time series between SLP, V850, Z500, SST fields, and rainfall over the training period 1951–90; strongly correlated areas are denoted by rectangles. Areas with correlation coefficients exceeding 0.8 within the rectangles are identified to calculate indices forming potential predictors Z_{1D}–Z_{4D}; their details are listed in Table 3. It is evident that these four potential predictors are strongly associated with the interdecadal rainfall variation with correlation coefficients ranging from −0.90 to −0.95, significant at the 0.01 level after adjusting the degree of freedom.

Figure 4b shows the CVSR screening procedure for calibrating the IDM. The significantly correlated well-known indices (SAM_D and PDO_D) are preferentially selected. At step 1, SAM_D is selected because of its smaller CV_RMSE value. Then there is no significant reduction in CV_RMSE value after sequential adding PDO_D at step 2 (*t*- and *F*-tests' values are 1.2 and 1.3, respectively, less than the significant values of 1.46 and 2.0 at the 0.15 level). The additional potential predictors Z_{1D}–Z_{4D} are added to be selected at the next steps. At step 3, together with SAM_D, sequential inclusion of Z_{1D} results in a statistically significant reduction in the CV_RMSE value to the minimum (*t*- and *F*-tests' values are 2.4 and 2.05); thus, Z_{1D} is selected as the second predictor. At step 4, the sequential inclusion of Z_{2D} reduces the CV_RMSE value to the minimum, but this reduction is not statistically significant, leading to the termination of the CVSR selecting procedure. SAM_D and Z_{1D} are selected into regression equation until now. However, the regression coefficient of SAM_D is not significant at the 0.05 level; the SAM_D is excluded. Finally, only Z_{1D} is taken as the predictor X_{1D} for the IDM given by

$$Y_D(t) = 320.5 - 47X_{1D}(t), \quad (3)$$

where $Y_D(t)$ is the interdecadal component of rainfall at *t*th year ($t = 1, \ldots, 40$) over 1951–90, and $X_{1D}(t)$ is the *t*th-observed values of the normalized X_{1D}.

Figure 5b shows the interdecadal variation of observed and downscaled rainfall from Eq. (3). Table 4 shows the correlation coefficients, RMSE, and the ratio of RMSE to the climatology rainfall. They are 0.95 and 16.2 mm (5.2%) in training period and 0.84 and 23.1 mm (7.5%) in test period, indicating a relative high skill in predicating the interdecadal variability using X_{1D}.

We now give an interpretation of why the predictor X_{1D} [i.e., the interdecadal component of June SLP over southwestern Indian Ocean (IO)] is associated with the interdecadal rainfall variation. In the past 50 years, X_{1D} has a pronounced increasing trend (Fig. 9 d). Figure 9a shows the interdecadal correlation of the detrended time series between X_{1D} and June surface temperature field, revealing the positive association between X_{1D} and the

TABLE 4. Downscaled results obtained from the interannual model (IAM) and interdecadal model (IDM) and their combination for total rainfall (total) in training period (1951–90) and independent test period (1991–2008). Cor. is correlation between observation and prediction; ρ is the ratio of RMSE (mm) to the climatology July–August rainfall during 1951–2008.

	Training period			Test period		
Model	Cor.	RMSE	ρ	Cor.	RMSE	ρ
IAM	0.76	34.2	11.1%	0.71	42.8	13.9%
IDM	0.95	16.2	5.2%	0.84	23.1	7.5%
Total	0.83	39.5	12.8%	0.82	45.8	14.8%

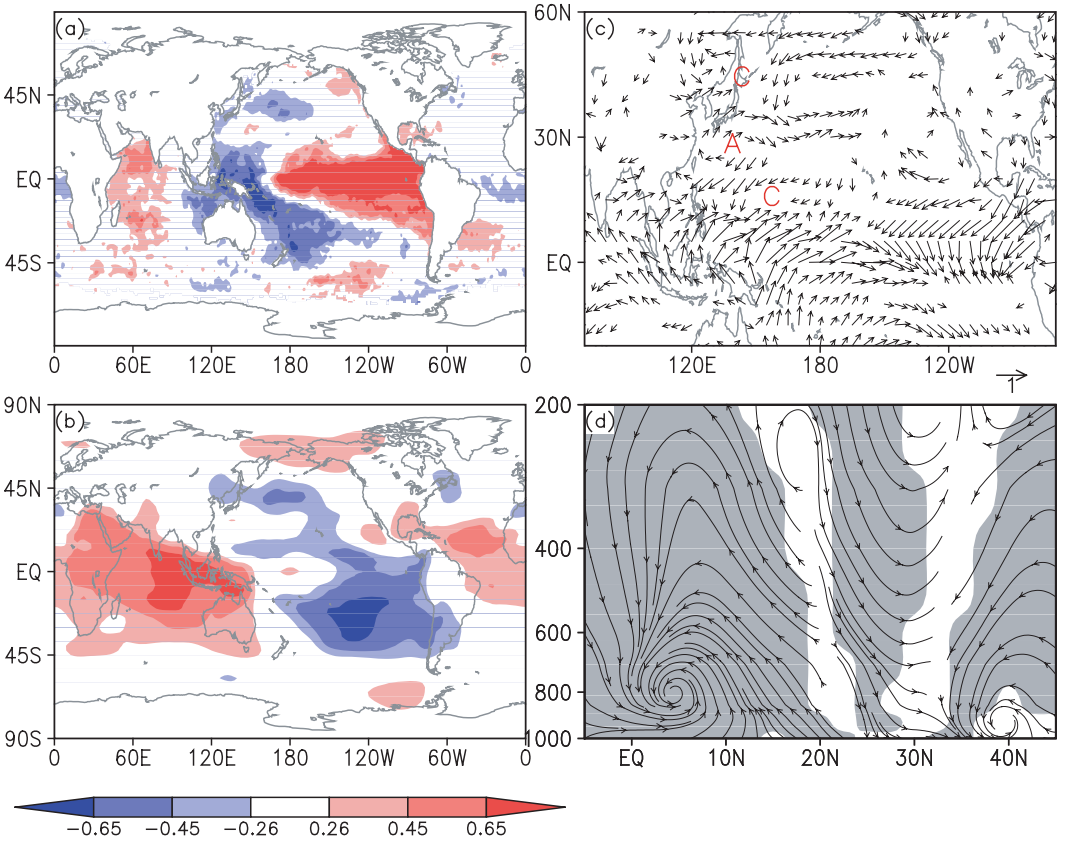

FIG. 6. Correlation of detrended time series between X_{1A} and interannual variability of (a) surface temperature, (b) 850-hPa geopotential height, (c) surface horizontal winds, and (d) meridional circulation along a latitude–pressure cross section averaged over 100°–140°E in July–August during 1951–2008. Shading and vectors drawn indicate significance at the 0.05 level. (c) Markers C and A denote anomalous cyclone and anticyclone, respectively.

surface temperature over western tropical Pacific and eastern tropical IO (i.e., the warm pool). Since the tropical IO has undergone anomalous warming during the past decades as indicated in previous studies (Ding et al. 2010; Du and Xie 2008; Li et al. 2008; Zhou et al. 2009a,b), it is likely to trigger the multidecadal increase in SLP over the southwestern IO via an anomalous zonal circulation. On the other hand, the ocean is a slowly varying medium and the warming anomaly over the warm pool may be responsible for the persistent X_{1D} anomaly and anomalous circulation over East Asia throughout the following JA.

Figure 9b presents the associated June surface circulation with positive X_{1D} anomaly. Associated with SLP increase over the southwestern IO, there appear anomalous northward cross-equatorial flows at about 50°–70°E longitudes. Meanwhile, the anomalous warming over the warm pool favors an anomalous northerly appearing over East China as reported by previous studies (Li et al. 2010; Zhou et al. 2009b). The anomalous northerly encounters the enhanced cross-equatorial southerly, intensifying the convergence in the intertropical convergence zone over the western Pacific. The enhanced convergence and ascent strengthens the meridional circulation, which is clearly seen in a latitude–vertical section averaged at 100°–140°E longitudes (Fig. 9c). The anomalous meridional circulation leads NC under a descent control and a shortage of moisture, leading to a dry summer. Figure 9d shows the normalized time series and linear trends of X_{1D} as well as the interdecadal rainfall component, clearly indicating their out-of-phase relationship.

c. *Downscaled total summer rainfall over NC*

It is straightforward to obtain the downscaled total rainfall by summing up downscaled values from IAM and the IDM. Figure 5c compares the downscaled and observed NC summer rainfall. Because the IAM and IDM are derived using data over the training period 1951–90, the predicted values after 1990 therefore indicate the true predictive skill. In general, the performance of the TSD approach evident in the training period is maintained during the subsequent verification period. Compared to the observed climatology rainfall

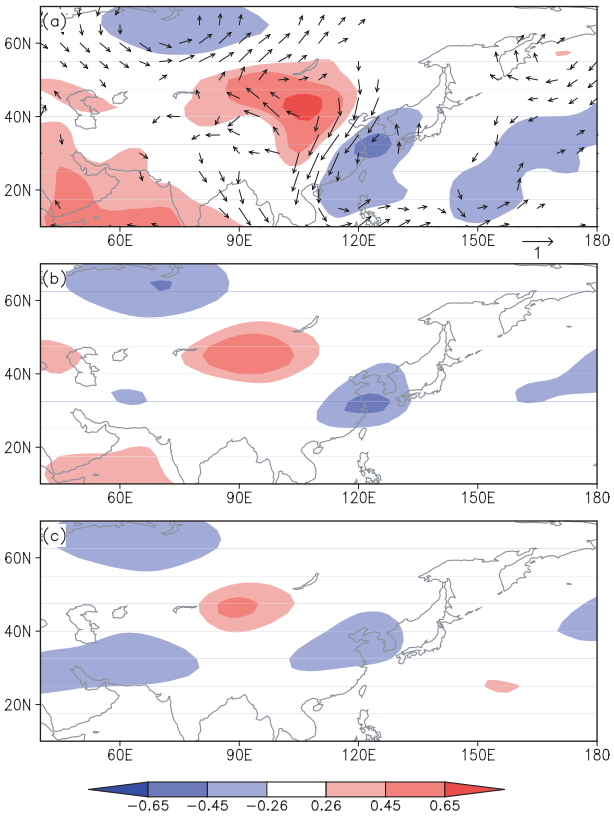

FIG. 7. Correlation of detrended time series between negative X_{2A} and interannual variability of (a) geopotential height (shading) and horizontal winds (vectors) at 850 hPa, (b) 500-hPa geopotential height, and (c) 200-hPa geopotential height in July–August during 1951–2008. Shading and vectors drawn indicate significance at the 0.05 level.

of 320.5 and 282.8 mm during 1951–90 and 1991–2008 periods, the downscaled results provide an accurate reproduction of 320.4 and 280.4 mm, respectively. Table 4 summarizes downscaling skill by showing some quantitative measurements. The correlation coefficients between the downscaled and observed rainfall are all highly significant at the 0.01 level, 0.83 for the training period, and 0.82 for the test period. RMSE (the ratio of RMSE to the climatology rainfall) is 39.5 mm (12.8%) in training period and 45.8 mm (14.8%) in test period. All of the results indicate that the TSD approach performs well on downscaling NC summer rainfall.

On the other hand, we have also compared the downscaling skills between the TSD approach and the single model (non-time-scale decomposition) based on C_CVSR downscaling scheme by Guo et al. (2011, manuscript submitted to *J. Geophys. Res.*). It is found that the TSD approach has a better skill in terms of higher correlation (0.82 versus 0.59) and a lower RMSE (45.8 versus 60.8 mm) between downscaled and observed rainfall in test period 1991–2008. This progress in prediction demonstrates the superiority of the TSD model.

5. Application to climate change simulations

We apply the downscaling models to predictors derived from GCMs' simulations for both the present-day and future climate. Before the application, we evaluate GCMs' simulation for predictors used in the IAM and IDM and select the well-performed GCMs to be utilized. This examination involves 21 GCMs in CMIP3, and only three GCMs (CSIRO Mk3.5, CNRM-CM3, and MPI ECHAM5) are selected finally on the basis that they are able to simulate the long-term-mean values and linear trends of the predictors well. Table 5 lists the results of the simulations of all predictors in present-day and future climate under A1B emission scenario from three selected GCMs and their ensemble mean. With the GCM-generated predictors, rainfall is estimated for the present-day climate (1951–99) and the near-future climate (2010–24 and 2035–49) under A1B emission scenario.

To downscale GCMs' outputs to NC summer rainfall, we update the IAM and IDM with observed rainfall and NCEP data from 1951 to 2008. GCM-generated predictors are placed in the updated forecast equations to make predictions. Figure 10 compares observed, GCMs directly predicted, and downscaled long-term-mean rainfall for 1951–99, 2010–24, and 2035–49. The downscaled value for the future is accompanied by 50% and 95% confidence intervals (horizontal lines in Fig. 10), which indicate the uncertainty associated with the downscaling model as estimated by bootstrap approach.

For predictions under the present-day climate (1951–99), all of the raw GCMs obviously underestimate the rainfall, while the downscaled values represent slight overestimates. Compared with the raw GCMs' simulations, in all cases, the downscaled values have a smaller percentage error: CSIRO Mk3.5 (+3% cf. −12%), CNRM-CM3 (+14% cf. −25%), MPI ECHAM5 (+17% cf. −21%), and ensemble mean (+11% cf. −19%).

For the future projection, simulations from CNRM-CM3, MPI ECHAM5, and the ensemble mean directly project a slow decrease in rainfall until 2010–24, followed by a slight increase (approaching the present-day state) until 2035–49, while CSIRO Mk3.5 indicates an opposite projection. However, the downscaled values show different projections from the raw GCMs' estimates. Except for the downscaled values based on MPI ECHAM5 that indicate a continuous decrease in rainfall, other downscaled values indicate a slight increase until 2010–24, followed by a slight decrease (still wetter than the present-day state) until 2035–49. The result indicates that there is a less chance for large changes to

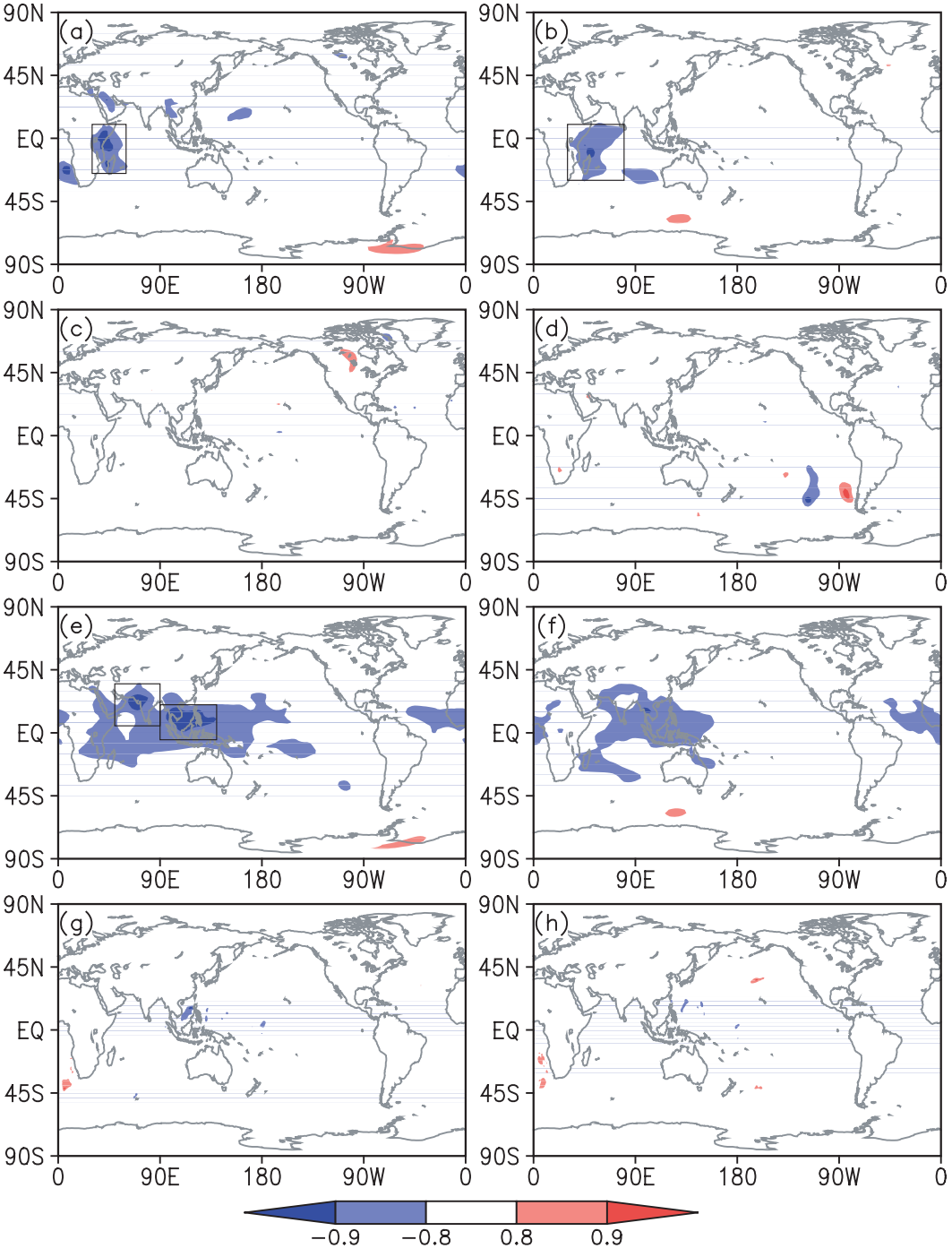

FIG. 8. As in Fig. 3, but on the interdecadal time scale.

happen, such as severe long-term droughts or floods (relative to the present-day state) for the next 40 years under A1B emission scenario. The wetting condition predicted by a majority of downscaled values is consistent with the prediction from the regional climate model (Gao et al. 2008), giving rise to more confidence to this projection.

6. Summary and discussion

In this paper, we have proposed a TSD approach to downscale NC summer rainfall through modeling the interannual and interdecadal rainfall variability by the IAM and IDM, respectively. The interannual components of June Niño-3 index and JA meridional wind over

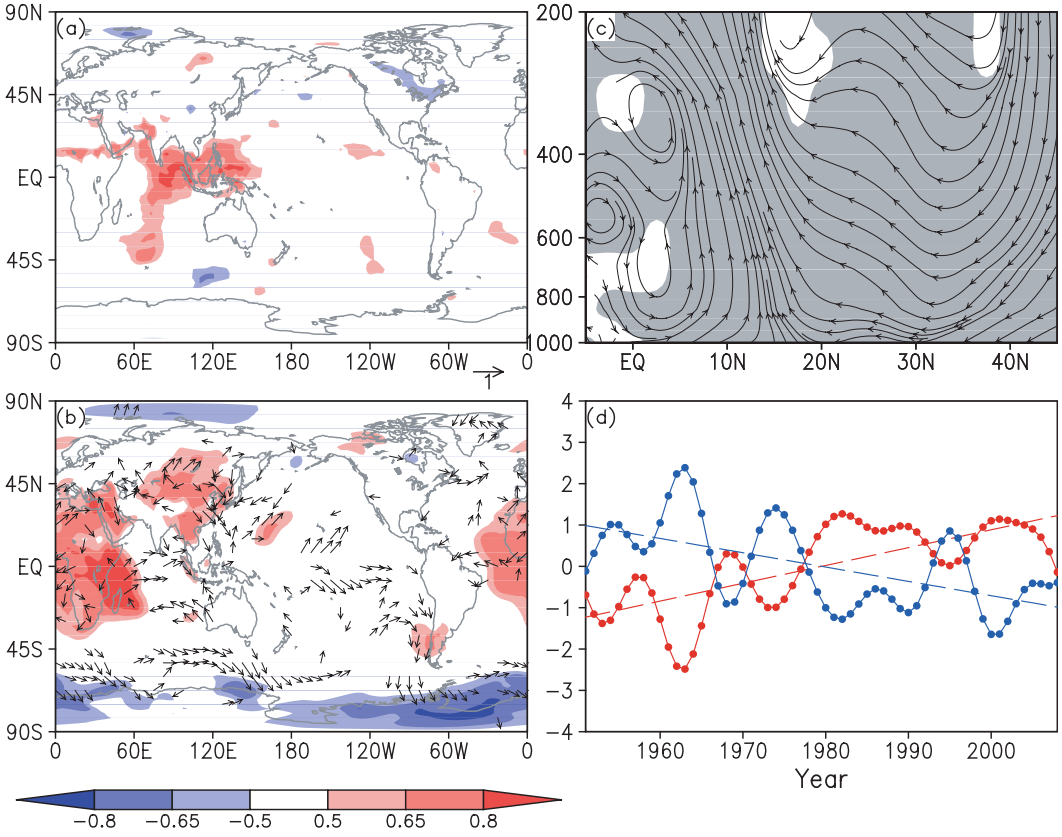

FIG. 9. Correlation of detrended time series between X_{1D} and interdecadal variability of (a) surface air temperature, (b) sea level pressure (shading) and surface winds (vectors) in June, and (c) meridional circulation along a latitude–pressure cross section averaged over 100°–140°E in July–August during 1951–2008. Shading and vectors drawn indicate significance at the 0.05 level. (d) Normalized time series (dotted line) and the associated linear trend (dash line) of X_{1D} (red) and North China summer rainfall (blue) during 1951–2008.

East China were linked to the interannual rainfall variability by the IAM, while the interdecadal component of SLP over the southwestern IO was linked to the interdecadal rainfall variability by the IDM. Both the IAM and IDM show good skills to downscale the interannual and interdecadal rainfall variability in NC summer rainfall. The downscaled total rainfall can be obtained by summing up the two downscaled components from the IAM and IDM. The results indicated that the TSD approach has a relatively high predictive capability for NC summer rainfall.

We have also applied the downscaling model to GCM-generated predictors and estimated the long-term rainfall conditions for both the present-day (1951–99) and the near-future climates (2010–24 and 2035–49) under A1B emission scenario. For the present-day climate, in all cases, the downscaled values showed smaller percentage errors than did the raw GCMs' simulations. This superiority indicated that the downscaled predictions are more reliable for representing the present-day climate, thus implying a better representation of the future climate. For future projection, a majority of downscaled values indicated a slight increase in rainfall, different from the raw GCMs' projection. The result also indicated that there would be less chance for large changes to happen, such as severe long-term droughts or floods (relative to the present-day state) for the next 40 years under A1B emission scenario.

We point out that the downscaling models in this study were calibrated based on NCEP-1 reanalysis data. Since the NCEP-1 data may have systematic errors in the period before 1970 (Greatbatch and Rong 2006), there is a need to verify the reliability of the proposed downscale models using other reanalysis data. We have repeated the same analysis by using 40-yr European Centre for Medium-Range Weather Forecasts (ECMWF) Re-Analysis (ERA-40) data (1958–2002) extended with NCEP-1 reanalysis data (2003–08). For IAM, the results based on these two distinct datasets were almost the same; for IDM, the area of predictor selected based on ERA-40 data relatively shrunk, and the downscaling skill was slightly worse. Anyhow, the downscaling models calibrated from these two reanalysis datasets showed

TABLE 5. Observed and GCM-simulated predictors (for definitions of predictors, see text) in terms of climatology values [X_{1A} (°C), X_{2A} (m s^{-1}) and X_{1D} (hPa)] and linear trend [X_{1A} (°C yr^{-1}), X_{2A} (m s^{-1} yr^{-1}) and X_{1D} (hPa yr^{-1})] during 1951–99 for the present-day climate and GCM-simulated climatology value during 2010–24 and 2035–49 for changed climate under A1B emission scenario.

		1951–99		2010–24	2035–49
Observation/GCMs	Predictors	Trend	Climatology	Climatology	Climatology
Observation	X_{1A}	−0.002	0.0		
	X_{2A}	−0.007	0.0		
	X_{1D}	0.034	1015.15		
CSIRO MK3.5	X_{1A}	0.004	0.0	−0.028	−0.011
	X_{2A}	0.0	0.0	0.069	−0.007
	X_{1D}	0.0	1015.00	1014.72	1014.84
CNRM-CM3	X_{1A}	0.006	0.0	−0.173	0.076
	X_{2A}	−0.002	0.0	0.011	−0.023
	X_{1D}	0.006	1014.49	1014.48	1014.39
MPI ECHAM5	X_{1A}	−0.001	0.0	0.082	0.029
	X_{2A}	−0.002	0.0	0.012	−0.004
	X_{1D}	0.010	1014.33	1014.41	1014.61
Ensemble mean	X_{1A}	0.003	0.0	−0.040	0.032
	X_{2A}	−0.001	0.0	0.031	−0.012
	X_{1D}	0.006	1014.61	1014.54	1014.61

similar skills to some extent, suggesting reliability of our downscaled results.

One should keep in mind that the reliability of downscaled future projection is strongly dependent on the GCMs' simulations of predictors. Hence, it is important to evaluate GCMs' simulations of predictors. In an evaluation of the 21 GCMs participating in CMIP3 regarding the predictors used both in the IAM and IDM, large

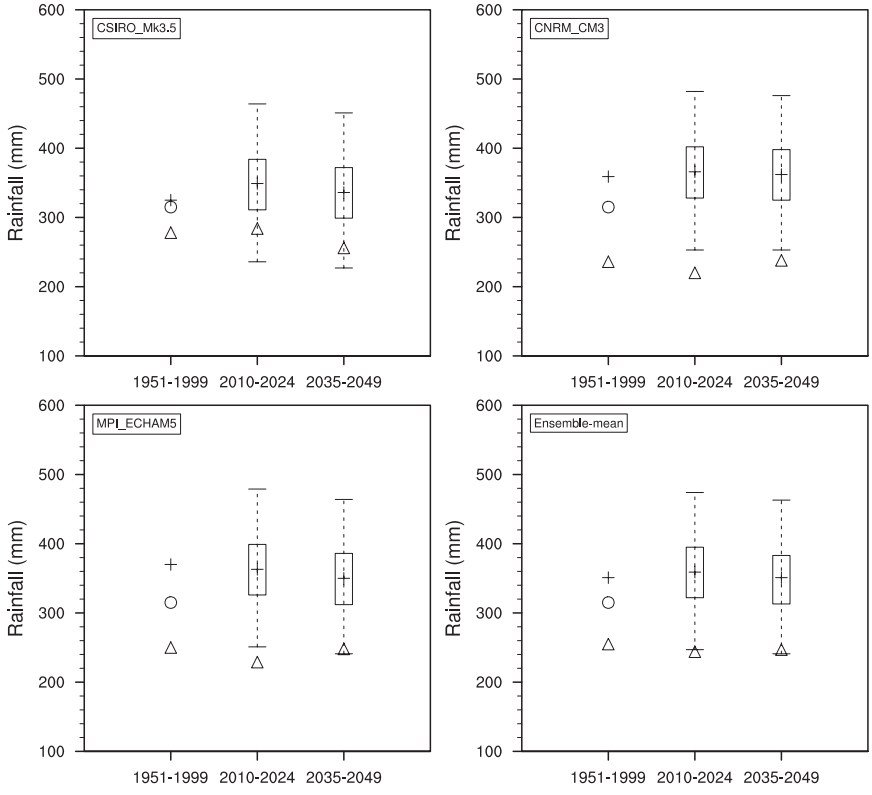

FIG. 10. Present-day (1951–99) and near-future (2010–24 and 2035–49) rainfall (mm) under A1B emission scenario from three GCMs and (bottom right) their ensemble mean. Circles represent observation, triangles represent raw GCMs' output, and crosses represent downscaled values. Boxes and error bars represent 50% and 95% confidence intervals, respectively.

errors were found in terms of the long-term-mean value, linear trend, and interannual variability. Therefore, the improvement of GCMs' simulations is important for statistical downscaling technique to obtain reliable projections.

It should be noted that the downscaled method in this paper only represented the changes in rainfall that linked to the changes in circulation. Previous studies have indicated the necessity to include the humidity-related parameters in projecting future rainfall changes because moisture would markedly change corresponding to future changes in radiation forcing (Benestad 2001; Charles et al. 1999; Crane and Hewitson 1998; Karl et al. 1990; Spak et al. 2007; Von Storch et al. 1993). In the present analysis, some changes in humidity may be accounted for by changes in the circulation field as they may affect the direction of moisture transfer; however, they would not account for large-scale changes in humidity associated with global warming. The latter effect is difficult to incorporate here because GCMs are unable to supply reliable simulations of the humidity-related predictor that was selected by correlation analysis.

Like other statistical downscaling models, the underlying stationary hypothesis may be questionable. Previous studies have emphasized the importance of assessing the robustness of the relationship in the future (Paul et al. 2008; Wilby and Wigley 1997). The statistical downscaling models that were linked with the principal climate modes try to test the persistence of the principal climate modes under changed climate conditions; however, this task cannot be performed in our downscaling model because it seeks predictors based on correlation analysis. Nevertheless, it is noteworthy that the relationship established in this paper is physically interpretable, which strengthens our confidence in the downscaled results for future.

Finally, it should be cautious to interpret the downscaled rainfall projections for future because the projections inevitably contain a degree of uncertainty. A consistent projection with additional types of downscaling models or regional climate models wound provide more reliability. Future work will make projection under other emission scenarios, such as A2 and B1, to obtain various rainfall conditions under distinct emission scenarios.

Acknowledgments. We acknowledge the international modeling groups for providing their data for analysis, the Program for Climate Model Diagnosis and Intercomparison (PCMDI) for collecting and achieving the model data, and the World Climate Research Programme's (WCRP's) Coupled Model Intercomparison Project for organizing the model data analysis activity. We thank two anonymous reviewers for comments. This work is jointly supported by the 973 Program (2010CB950400), NSFC Key Project (41030961), and the Australia-China Bilateral Climate Change Partnerships Program of the Australian Department of Climate Change. Yun Li was also supported by the Indian Ocean Climate Initiative Project of Western Australian State Government.

APPENDIX A

Cross-Validation-Based Stepwise Regression Approach

The CVSR approach is a ''forward'' stepwise screening procedure to select the ''optimal'' predictors from the potential predictor set. It employs leave-one-out cross validation to select the robust predictors and reduce the false possibility. The root-mean-square error between observation and cross-validation estimates (CV_RMSE) is taken as the criterion to evaluate the performance of potential predictor.

The CVSR method can be described in a general form using a series of iteration steps:

$$Y(t) = c + \sum_{i=1}^{p} \beta_i X_i(t) + \varepsilon(t), \tag{A1}$$

where $Y(t)$ is the predictand for $t = 1, \ldots, n$ year training period; $X_i(t)$ is the tth observation of the predictor X_i selected from candidate predictors $Z_1, \ldots, Z_m$ by the ith step in forward stepwise regression screening; c and β_i are model parameters; and $\varepsilon(t)$ is the error of the estimated model (A1). Specifically, model (A1) is established by the following $p < m$ steps.

- Step 1: Regress the predictand $Y(t)$ onto each of the potential predictors Z_{i_1} ($i_1 \in \{1, \ldots, m\}$) to obtain 1-predictor regression equation f_{i_1}. The performance of each 1-predictor regression equation is measured by CV_RMSE at step 1

$$\text{CV\_RMSE}_{i_1} = \sqrt{\frac{1}{n}\sum_{t=1}^{n}\{Y(t) - f_{i_1,-t}[Z_{i_1}(t)]\}^2}, \tag{A2}$$

where regression equation $f_{i_1,-t}$ is fitted by $Z_{i_1}(j)$ ($j \in \{1, \ldots, n\}\backslash\{t\}$), that is, all observations excluding the tth one. If CV_RMSE_{i_1} is the smallest CV_RMSE achieved at step 1, that is, $\text{CV\_RMSE}_1 = \min_{i_1 \in \{1,\ldots,m\}}\{\text{CV\_RMSE}_{i_1}\}$, the potential predictor Z_{i_1} is selected as the first predictor, that is, $X_1 = Z_{i_1}$.

- Step 2: Regress $Y(t)$ onto X_1 and each of the remaining m-1 potential predictors $Z_{i_2}(i_2 \in \{1, \ldots, m\}\backslash\{i_1\})$, that is, all potential predictors except Z_{i_1} to write 2-predictor regression equation f_{i_2}. The performance of each 2-predictor regression equation is measured by CV_RMSE at step 2

$$\mathrm{CV\_RMSE}_{i_2} = \sqrt{\frac{1}{n}\sum_{t=1}^{n}\{Y(t) - f_{i_2,-t}[X_1(t), Z_{i_2}(t)]\}^2}, \tag{A3}$$

where regression equation $f_{i_2,-t}$ is fitted by $X_1(j)$, $Z_{i_2}(j)(j \in \{1, \ldots, n\}\backslash\{t\})$. Now, if $\mathrm{CV\_RMSE}_{i_2}$ is the smallest CV_RMSE achieved at step 2, that is, $\mathrm{CV\_RMSE}_2 = \min_{i_2 \in \{1,\ldots,m\}\backslash\{i_1\}}\{\mathrm{CV\_RMSE}_{i_2}\}$ and moreover, $\mathrm{CV\_RMSE}_2$ is significantly smaller than $\mathrm{CV\_RMSE}_1$, the potential predictor Z_{i_2} is selected as the second predictor, that is, $X_2 = Z_{i_2}$; otherwise, stop selecting new predictors. To statistically test the significant reduction in $\mathrm{CV\_RMSE}_2$ relative to $\mathrm{CV\_RMSE}_1$, t and F tests are utilized to test the quadratic errors series between the observation and cross-validated estimates obtained at step 2 [i.e., $\{Y(t) - f_{2,-t}[X_1(t), X_2(t)]\}^2, t \in \{1, \ldots, n\}$, where $f_{2,-t}$ is fitted by $X_1(j), X_2(j), (j \in \{1, \ldots, n\}\backslash\{t\})$] and at step 1 [i.e., $\{Y(t) - f_{1,-t}[X_1(t)]\}^2, t \in \{1, \ldots, n\}$, where $f_{1,-t}$ is fitted by $X_1(j), (j \in \{1, \ldots, n\}\backslash\{t\})$] in terms of the mean value and the variance.

Generally, at step k, assume that there is $k - 1$ predictors $X_1 = Z_{i_1}, \ldots, X_{k-1} = Z_{i_{k-1}}$ selected from original potential predictors $Z_1, \ldots, Z_m$, and the associated smallest CV_RMSE at step $k - 1$ is

$$\mathrm{CV\_RMSE}_{k-1} = \min_{i_{k-1} \in \{1,\ldots,m\}\backslash\{i_1,\ldots,i_{k-2}\}} \sqrt{\frac{1}{n}\sum_{t=1}^{n}\{Y(t) - f_{i_{k-1},-t}[X_1(t), \ldots, X_{(k-2)}(t), Z_{i_{k-1}}(t)]\}^2}, \tag{A4}$$

where regression equation $f_{i_{k-1},-t}$ is fitted by $X_1(j), \ldots, X_{(k-2)}(j), Z_{i_{k-1}}(j), (j \in \{1, \ldots, n\}\backslash\{t\})$.

Step k: Regress $Y(t)$ onto $X_1, \ldots, X_{k-1}$ and each $Z_{i_k}(i_k \in \{1, \ldots, m\}\backslash\{i_1, i_2, \ldots, i_{k-1}\})$ of remaining m-$(k-1)$ potential predictors to write k-predictor regression equation f_{i_k}. The performance of each k-predictor regression equation is measured by CV_RMSE at step k

$$\mathrm{CV\_RMSE}_{i_k} = \sqrt{\frac{1}{n}\sum_{t=1}^{n}\{Y(t) - f_{i_k,-t}[X_1(t), \ldots, X_{(k-1)}(t), Z_{i_k}(t)]\}^2}, \tag{A5}$$

where regression equation $f_{i_k,-t}$ is fitted by $X_1(j), \ldots, X_{(k-1)}(j), Z_{i_k}(j), (j \in \{1, \ldots, n\}\backslash\{t\})$. If $\mathrm{CV\_RMSE}_{i_k}$ is the smallest CV_RMSE achieved at step k, that is, $\mathrm{CV\_RMSE}_k = \min_{i_k \in \{1,\ldots,m\}\backslash\{i_1,\ldots,i_{k-1}\}}\{\mathrm{CV\_RMSE}_{i_k}\}$ and moreover, $\mathrm{CV\_RMSE}_k$ is significantly smaller than $\mathrm{CV\_RMSE}_{k-1}$, the potential predictor Z_{i_k} is selected as the kth predictor, that is, $X_k = Z_{i_k}$; otherwise, stop selecting new predictors. The t and F tests are utilized to statistically test the quadratic errors series between the observation and cross-validated estimates obtained at step k [i.e., $\{Y(t) - f_{k,-t}[X_1(t), \ldots, X_k(t)]\}^2, t \in \{1, \ldots, n\}$, where $f_{k,-t}$ is fitted by $X_1(j), \ldots, X_k(j), (j \in \{1, \ldots, n\}\backslash\{t\})$] and at step k-1 [i.e., $\{Y(t) - f_{k-1,-t}[X_1(t), \ldots, X_{k-1}(t)]\}^2, t \in \{1, \ldots, n\}$, where $f_{k-1,-t}$ is fitted by $X_1(j), \ldots, X_{k-1}(j), (j \in \{1, \ldots, n\}\backslash\{t\})$] in terms of the mean value and the variance.

Finally, for all of the selected predictors via the CVSR procedure, F test is used to test their regression coefficients. The insignificant predictors wound be excluded, and the remaining predictors are used to fit the multilinear-regression equation with the least squares method.

APPENDIX B

Bootstrapping Prediction Intervals for Linear Regression Model

In general, a linear regression model is defined as

$$Y(t) = \sum_{k=1}^{p}\beta_k X_k(t) + \varepsilon_t, \tag{B1}$$

where ε_t is residual error. Least squares fit to the n-yr training data $\{[\mathbf{X}(t), Y(t)]: t = 1, \ldots, n\}$ yields

$$\hat{Y}(t) = \sum_{k=1}^{p}\hat{\beta}_k X_k(t). \tag{B2}$$

It is validated by using independent data $\{[(\mathbf{X}(t + h), Y(t + h)]: h = 1, \ldots, N - n\}(N > n)$. To quantify the uncertainty of downscaled rainfall using Eq. (B2) related to $X_i(t + h)$ $(i = 1, \ldots, p; h = 1, \ldots, N - n)$, we need to establish the cumulative distribution function G

for the confidence interval of the prediction error $Y(t+h) - \hat{Y}(t+h)$. A $100(1-\alpha)\%$ prediction intervals for $Y(t+h)$ is given by

$$[\hat{Y}(t+h) + G^{-1}(\alpha/2), \hat{Y}(t+h) + G^{-1}(1-\alpha/2)]. \quad \text{(B3)}$$

However, as the distribution F of the residual variability ε_t in Eq. (B1) is unknown, we cannot obtain the distribution G analytically. We apply a bootstrap-resampling procedure to estimate the distribution G.

First, the residuals $e_t = Y(t) - \hat{Y}(t)$ are calculated with Eq. (B2). For an independent test data $\{\mathbf{X}(t+h), h = 1, \ldots, N-n\}$, predicted value $\hat{Y}(t+h) = \sum_{k=1}^{p} \hat{\beta}_k X_k(t+h)$. The error distribution F is estimated by the empirical distribution of residuals, which we denote F_n. This is then used to construct bootstrapped samples of the form

$$\{[\mathbf{X}(t), Y^*(t)]\}, \quad t = 1, \ldots, n, \quad [\mathbf{X}(t+h), Y^*(t+h)],$$

with $Y^*(t) = \hat{Y}(t) + \varepsilon_t^*$ and $Y^*(t+h) = \hat{Y}(t+h) + \varepsilon'^*_t$, where ε_t^* and ε'^*_t are independently sampled from F_n, that is, they are randomly sampled with replacement from the set of residuals $\{e_1, \ldots, e_n\}$. The superscript * denotes a value constructed for a particular bootstrap sample.

Each bootstrapped sample is used to calculate a simulated estimate $\hat{\beta}_k^*$, predicted value $\hat{Y}^*(t+h)$, and predicted error $\varepsilon'^*_t = Y^*(t+h) - \hat{Y}^*(t+h)$. The empirical distribution of ε'^*_t, which we denote $\tilde{G}$, is then an estimate of the distribution of the bootstrap prediction errors. It can be used as the distribution function G. Therefore, a $100(1-\alpha)\%$ prediction interval for $Y(t+h)$ can be estimated as

$$[\hat{Y}(t+h) + \tilde{G}^{-1}(\alpha/2), \hat{Y}(t+h) + \tilde{G}^{-1}(1-\alpha/2)].$$

In our downscaling rainfall analysis, estimates of the 95% confidence interval of predicted rainfall for 1000 bootstrapping samples using independent test data over 1991–2008 are shown as dashed blue curves in Fig. 5c. Further, bootstrapping estimates of the uncertainty (50% and 95% confidence intervals for 1000 bootstrap replications) of downscaled future rainfall are shown in Fig. 10.

REFERENCES

Benestad, R. E., 2001: A comparison between two empirical downscaling strategies. *Int. J. Climatol.,* **21,** 1645–1668.

——, 2002: Empirically downscaled multimodel ensemble temperature and precipitation scenarios for Norway. *J. Climate,* **15,** 3008–3027.

——, 2004: Empirical-statistical downscaling in climate modeling. *Eos, Trans. Amer. Geophys. Union,* **85,** 417–422.

Bergant, K., and L. Kajfe-Bogataj, 2005: N-CPLS regression as empirical downscaling tool in climate change studies. *Theor. Appl. Climatol.,* **81,** 11–23.

Busuioc, A., D. Chen, and C. Hellstrom, 2001: Performance of statistical downscaling models in GCM validation and regional climate change estimates: Application for Swedish precipitation. *Int. J. Climatol.,* **21,** 557–578.

Charles, S. P., B. C. Bates, P. H. Whetton, and J. P. Hughes, 1999: Validation of downscaling models for changed climate conditions: Case study of southwestern Australia. *Climate Res.,* **12,** 1–14.

Crane, R. G., and B. C. Hewitson, 1998: Doubled CO_2 precipitation changes for the Susquehanna Basin: Downscaling from the Genesis general circulation model. *Int. J. Climatol.,* **18,** 65–76.

Ding, R., K. J. Ha, and J. Li, 2010: Interdecadal shift in the relationship between the East Asian summer monsoon and the tropical Indian Ocean. *Climate Dyn.,* **34,** 1059–1071.

Ding, Y., Y. Sun, Z. Wang, Y. Zhu, and Y. Song, 2009: Interdecadal variation of the summer precipitation in China and its association with decreasing Asian summer monsoon Part II: Possible causes. *Int. J. Climatol.,* **29,** 1926–1944.

Du, Y., and S. Xie, 2008: Role of atmospheric adjustments in the tropical Indian Ocean warming during the 20th century in climate models. *Geophys. Res. Lett.,* **35,** L08712, doi:10.1029/2008GL033631.

Fowler, H. J., S. Blenkinsop, and C. Tebaldi, 2007: Linking climate change modelling to impacts studies: Recent advances in downscaling techniques for hydrological modelling. *Int. J. Climatol.,* **27,** 1547–1578.

Frias, M. D., E. Zorita, J. Fernandez, and C. Rodriguez-Puebla, 2006: Testing statistical downscaling methods in simulated climates. *Geophys. Res. Lett.,* **33,** L19807, doi:10.1029/2006GL027453.

Gao, X., Y. Shi, R. Song, F. Giorgi, Y. Wang, and D. Zhang, 2008: Reduction of future monsoon precipitation over China: Comparison between a high resolution RCM simulation and the driving GCM. *Meteor. Atmos. Phys.,* **100,** 73–86.

Greatbatch, R. J., and P. Rong, 2006: Discrepancies between different Northern Hemisphere summer atmospheric data products. *J. Climate,* **19,** 1261–1273.

Grotch, S. L., and M. C. MacCracken, 1991: The use of general circulation models to predict regional climatic change. *J. Climate,* **4,** 286–303.

Hanssen-Bauer, I., and E. J. Forland, 1998: Long-term trends in precipitation and temperature in the Norwegian Arctic: Can they be explained by changes in atmospheric circulation patterns? *Climate Res.,* **10,** 143–153.

Hoskins, B. J., and D. Karoly, 1981: The steady linear response of a spherical atmosphere to thermal and orographic forcing. *J. Atmos. Sci.,* **38,** 1179–1196.

Huang, R. H., and Y. Wu, 1989: The influence of ENSO on the summer climate change in China and its mechanism. *Adv. Atmos. Sci.,* **6,** 21–32.

——, G. Huang, and B. H. Ren, 1999: Advances and problems needed for further investigation in the studies of the East Asian summer monsoon (in Chinese). *Chin. J. Atmos. Sci.,* **23,** 129–141.

——, J. L. Cheng, G. Huang, and Q. L. Zhang, 2006: The Quasi-biennial oscillation of summer monsoon rainfall in China and its cause (in Chinese). *Chin. J. Atmos. Sci.,* **30,** 545–560.

——, L. Gu, J. L. Chen, and G. Huang, 2008: Recent progresses in studies of the temporal-spatial variations of the East Asian

monsoon system and their impacts on climate anomalies in China (in Chinese). *Chin. J. Atmos. Sci.,* **32,** 691–719.

Karl, T. R., W.-C. Wang, M. E. Schlesinger, R. W. Knight, and D. Portman, 1990: A method of relating general circulation model simulated climate to the observed local climate. Part I: Seasonal statistics. *J. Climate,* **3,** 1053–1079.

Kidson, J. W., and C. S. Thompson, 1998: A comparison of statistical and model-based downscaling techniques for estimating local climate variations. *J. Climate,* **11,** 735–753.

Li, J. P., and Q. C. Zeng, 2002: A unified monsoon index. *Geophys. Res. Lett.,* **29,** 1274, doi:10.1029/2001GL013874.

——, and J. Wang, 2003a: A modified zonal index and its physical sense. *Geophys. Res. Lett.,* **30,** 1632, doi:10.1029/2003GL017441.

——, and ——, 2003b: A new North Atlantic Oscillation index and its variability. *Adv. Atmos. Sci.,* **20,** 661–676.

——, Z. Wu, Z. Jiang, and J. He, 2010: Can global warming strengthen the East Asian summer monsoon? *J. Climate,* **23,** 6696–6705.

Li, S., J. Lu, G. Huang, and K. Hu, 2008: Tropical Indian Ocean basin warming and East Asian summer monsoon: A multiple AGCM study. *J. Climate,* **21,** 6080–6088.

Li, W. J., Z. G. Zhao, X. Li, and L. H. Sun, 2003: The drought characteristics analysis in North China and its causes of formation. *Arid Meteor.,* **21,** 1–5.

Li, Y., and I. Smith, 2009: A statistical downscaling model for southern Australia winter rainfall. *J. Climate,* **22,** 1142–1158.

Lu, R. Y., 2002: Separation of interannual and decadal variations of rainfall in North China (in Chinese). *Chin. J. Atmos. Sci.,* **26,** 611–624.

——, 2003: Linear relationship between the interdecadal and interannual variabilities of North China rainfall in rainy season. *Chin. Sci. Bull.,* **48,** 1040–1044.

——, 2005: Interannual variation of North China rainfall in rainy season and SSTs in the equatorial eastern Pacific. *Chin. Sci. Bull.,* **50,** 2069–2073.

Maxino, C., B. McAvaney, A. Pitman, and S. Perkins, 2008: Ranking the AR4 climate models over the Murray-Darling Basin using simulated maximum temperature, minimum temperature and precipitation. *Int. J. Climatol.,* **28,** 1097–1112.

Milly, P. C. D., J. Betancourt, M. Falkenmark, R. M. Hirsch, Z. W. Kundzewicz, D. P. Lettenmaier, and R. J. Stouffer, 2008: Climate change—Stationarity is dead: Whither water management? *Science,* **319,** 573–574.

Nan, S., and J. Li, 2003: The relationship between the summer precipitation in the Yangtze River valley and the boreal spring Southern Hemisphere annular mode. *Geophys. Res. Lett.,* **30,** 2266, doi:10.1029/2003GL018381.

Nitta, T., 1987: Convective activities in the tropical western Pacific and their impact on the Northern Hemisphere summer circulation. *J. Meteor. Soc. Japan,* **65,** 373–390.

Oshima, N., H. Kato, and S. Kadokura, 2002: An application of statistical downscaling to estimate surface air temperature in Japan. *J. Geophys. Res.,* **107,** 4095, doi:10.1029/2001JD000762.

Paul, S., C. M. Liu, J. M. Chen, and S. H. Lin, 2008: Development of a statistical downscaling model for projecting monthly rainfall over East Asia from a general circulation model output. *J. Geophys. Res.,* **113,** D15117, doi:10.1029/2007JD009472.

Perkins, S., A. Pitman, N. Holbrook, and J. McAneney, 2007: Evaluation of the AR4 climate models' simulated daily maximum temperature, minimum temperature, and precipitation over Australia using probability density functions. *J. Climate,* **20,** 4356–4376.

Schmidli, J., C. M. Goodess, C. Frei, M. R. Haylock, Y. Hundecha, J. Ribalaygua, and T. Schmith, 2007: Statistical and dynamical downscaling of precipitation: An evaluation and comparison of scenarios for the European Alps. *J. Geophys. Res.,* **112,** D04105, doi:10.1029/2005JD007026.

Smith, I., and E. Chandler, 2009: Refining rainfall projections for the Murray darling Basin of southeast Australia—The effect of sampling model results based on performance. *Climatic Change,* **102,** 1–17.

Solomon, S., and Coauthors, Eds., 2007: *Climate Change 2007: The Physical Science Basis*. Cambridge University Press, 996 pp.

Spak, S., T. Holloway, B. Lynn, and R. Goldberg, 2007: A comparison of statistical and dynamical downscaling for surface temperature in North America. *J. Geophys. Res.,* **112,** D08101, doi:10.1029/2005JD006712.

Stine, R. A., 1985: Bootstrap prediction intervals for regression. *J. Amer. Stat. Assoc.,* **80,** 1026–1031.

Sun, S. Q., 1999: A study on the features of drought and flood in North China in recent 50 years and relations between them and global changes (in Chinese). *Plateau Meteor.,* **18,** 541–551.

Timbal, B., A. Dufour, and B. McAvaney, 2003: An estimate of future climate change for western France using a statistical downscaling technique. *Climate Dyn.,* **20,** 807–823.

Von Storch, H., E. Zorita, and U. Cubasch, 1993: Downscaling of global climate change estimates to regional scales: An application to Iberian rainfall in wintertime. *J. Climate,* **6,** 1161–1171.

Wang, B., R. G. Wu, and X. H. Fu, 2000: Pacific–East Asian teleconnection: How does ENSO affect East Asian climate? *J. Climate,* **13,** 1517–1536.

——, Z. Wu, J. Li, J. Liu, C. P. Chang, Y. Ding, and G. Wu, 2008: How to measure the strength of the East Asian summer monsoon. *J. Climate,* **21,** 4449–4463.

Wang, H. J., and F. Xun, 2003: Interannual variability of Somali Jet and its influences on the interhemispheric water vapor transport and on the East Asian summer rainfall (in Chinese). *Chin. J. Geophys.,* **46,** 18–25.

Whetton, P. H., K. L. McInnes, R. N. Jones, K. J. Hennessy, R. Suppiah, C. M. Page, J. Bathols, and P. J. Durack, 2005: Australian climate change projections for impact assessment and policy application: A review. CSIRO Marine and Atmospheric Research Paper 1, 2008–2012.

Wilby, R. L., 1997: Non-stationarity in daily precipitation series: Implications for GCM downscaling using atmospheric circulation indices. *Int. J. Climatol.,* **17,** 439–454.

——, 1998: Statistical downscaling of daily precipitation using daily airflow and seasonal teleconnection indices. *Climate Res.,* **10,** 163–178.

——, and T. M. L. Wigley, 1997: Downscaling general circulation model output: A review of methods and limitations. *Prog. Phys. Geogr.,* **21,** 530.

——, and ——, 2000: Precipitation predictors for downscaling: Observed and general circulation model relationships. *Int. J. Climatol.,* **20,** 641–661.

Wu, Z., and J. Li, 2008: Prediction of the Asian–Australian monsoon interannual variations with the grid-point atmospheric model of IAP LASG (GAMIL). *Adv. Atmos. Sci.,* **25,** 387–394.

——, and ——, 2009: Seasonal prediction of the global precipitation annual modes with the grid-point atmospheric model of IAP LASG. *Acta Meteor. Sin.,* **23.**

——, B. Wang, J. Li, and F. Jin, 2009: An empirical seasonal prediction model of the east Asian summer monsoon using ENSO and NAO. *J. Geophys. Res.,* **114,** D18120, doi:10.1029/2009JD011733.

——, J. Li, Z. Jiang, J. He, and X. Zhu, 2011: Possible effects of the North Atlantic Oscillation on the strengthening relationship between the East Asian summer monsoon and ENSO. *Int. J. Climatol.,* doi:10.1002/joc.2309, in press.

Xia, J., L. Zhang, C. Liu, and J. Yu, 2007: Towards better water security in North China. *Water Resour. Manage.,* **21,** 233–247.

Xue, F., 2005: Influence of the southern circulation on East Asian summer monsoon (in Chinese). *Climate Environ. Res.,* **10,** 123–130.

Yang, H., and S. Q. Sun, 2003: Longitudinal displacement of the subtropical high in the western Pacific in summer and its influence. *Adv. Atmos. Sci.,* **20,** 921–933.

Zhang, Y., J. M. Wallace, and D. S. Battisti, 1997: ENSO-like interdecadal variability: 1900–93. *J. Climate,* **10,** 1004–1020.

Zhao, S. R., and Z. S. Song, 1999: Floods and droughts in northern China and general circulation anomalies over middle and high latitudes (in Chinese). *Plateau Meteor.,* **18,** 535–540.

Zhou, T. J., D. Y. Gong, J. Li, and B. Li, 2009a: Detecting and understanding the multi-decadal variability of the East Asian summer monsoon recent progress and state of affairs. *Meteor. Z.,* **18,** 455–467.

——, and Coauthors, 2009b: Why the western Pacific subtropical high has extended westward since the late 1970s. *J. Climate,* **22,** 2199–2215.

Zhu, C. W., C. K. Park, W. S. Lee, and W. T. Yun, 2008: Statistical downscaling for multi-model ensemble prediction of summer monsoon rainfall in the Asia–Pacific region using geopotential height field. *Adv. Atmos. Sci.,* **25,** 867–884.